

Dynamic Tensile Deformation of High Strength Aluminum Alloys Processed Following Novel Thermomechanical Treatment Strategies

Emad Scharifi,* Seyed Vahid Sajadifar, Ghazal Moeini, Ursula Weidig, Stefan Böhm, Thomas Niendorf, and Kurt Steinhoff

Herein, the effects of a very recently introduced novel thermomechanical process route on the microstructural evolution and dynamic tensile deformation behavior of two different precipitation hardenable aluminum alloys, i.e., AA6082 and AA7075, are studied. The investigated materials are hot formed and quenched in differently tempered tools to reveal the influence of cooling rate. Microstructure analysis is conducted to study the influences of different cooling strategies on the microstructure evolution and prevailing strengthening mechanisms in the investigated conditions. Dynamic tensile tests at strain rates of 40, 200, and 400 s⁻¹ coupled with digital image correlation are further conducted to study the mechanical performance and the local deformation behavior. Experimental results show a decrease in yield and tensile strength for the material quenched at higher tool temperature. With increasing strain rate, strength and elongation to failure of the investigated alloys increase for all conditions. The obtained mechanical properties can be rationalized based on the prevailing microstructural features. Both alloys show fine and well-distributed precipitates upon fast quenching, whereas coarse precipitates prevail upon slow cooling.

challenge, different engineering materials were studied and are used to meet global trends toward intense CO₂ reduction.^[2–5] Still, this scenario promotes an enormous effort and numerous novel solutions to produce light components with superior mechanical properties. Aluminum and its alloys were found to be an outstanding candidate for applications demanding lightweight design and adequate performance due to their excellent strength-to-weight ratio.^[4] To realize complex-formed thin-walled structures, a multitude of forming processes have to be applied to treat the alloys and sheet materials in focus.^[6,7] The sheet forming strategies developed for high-strength aluminum alloys require high dynamic forces. Further, they include several deformation steps and strain paths, eventually leading to various detrimental effects, such as springback, local thinning, damage nucleation, damage propagation,

1. Introduction


Over the past decades, lightweight design became one of the main subjects in the transportation sector.^[1] To address this

and so forth.^[8,9] These effects are caused by the limited formability and the corresponding elastic–plastic behavior of high-strength aluminum alloys, particularly at room temperature. To overcome these challenges, a novel thermomechanical forming route, which was first proposed by Lin et al.,^[10] offers pathways toward an superior formability, concomitantly reducing springback in the final geometry. For this reason, this method has gained significant interest of aluminum suppliers and, thus, is the topic of numerous current scientific works.^[11–15]

E. Scharifi, Dr. U. Weidig, Prof. K. Steinhoff
Metal Forming Technology
University of Kassel
Kurt-Wolters-Straße 3, Kassel 34125, Germany
E-mail: emad.scharifi@uni-kassel.de

Dr. S. V. Sajadifar, Prof. T. Niendorf
Institute of Materials Engineering
University of Kassel
Mönchebergstraße 3, Kassel 34125, Germany

Dr. G. Moeini, Prof. S. Böhm
Department for Cutting and Joining Manufacturing Processes
University of Kassel
Kurt-Wolters-Straße 3, Kassel 34125, Germany

 The ORCID identification number(s) for the author(s) of this article can be found under <https://doi.org/10.1002/adem.202000193>.

© 2020 The Authors. Published by WILEY-VCH Verlag GmbH & Co. KGaA, Weinheim. This is an open access article under the terms of the Creative Commons Attribution License, which permits use, distribution and reproduction in any medium, provided the original work is properly cited.

DOI: 10.1002/adem.202000193

The aforementioned approach for the forming of aluminum alloys combines solution heat treatment (SHT) and hot stamping including simultaneous cooling within the forming tools. In general, hot forming of aluminum alloys at temperatures well above room temperature increases the formability as is reported in numerous studies, e.g., the study by Li et al.^[16] The hot deformation behavior of AA2024 in a wide range of temperatures (350–493 °C) was investigated by Wang et al. using a Gleeble 3800.^[17] The results obtained in that study reveal a pronounced increase in total elongation with increasing deformation temperature up to 450 °C. This behavior was rationalized by thermally activated softening mechanisms. Therefore, this temperature was assumed to be the optimum forming temperature. At higher temperatures (e.g., 493 °C), the ductility of the investigated material decreased dramatically. A similar trend was observed

for AA2060. Upon increasing the temperatures to values above the optimum, a steep decrease in elongation to failure resulted.^[18] Further studies focusing on the hot forming process of complex-shaped components revealed high dimensional accuracy and less pronounced material thinning. Furthermore, similar mechanical properties as compared with the as-received (AR) T6 condition for heat treatable aluminum alloys were found.^[19–21] At the same time, the integrated process has been shown to be of highest interest for the forming of non-heat treatable aluminum alloys.^[22,23]

The novel approach offers a wide range of cooling strategies for tailoring various properties in case of heat treatable aluminum alloys. However, several challenges prevail in parallel: a complete dissolution of alloying elements during solution treatment, suppression of nucleation and growth of precipitates especially at the grain boundaries, preservation of the supersaturated state as well as perpetuation of the high concentration of vacancies by high cooling rates, are essential factors to be adequately addressed to set the final mechanical properties. The individually established metastable condition (by apt thermomechanical processing) promotes in case of precipitation-hardenable aluminum alloys, such as AA2xxx, AA6xxx, or AA7xxx series, the subsequent nucleation and growth of precipitations during an additional aging process at moderate temperatures.^[24] The most important specific condition, the so-called supersaturated solid solution, can robustly be established in the combined forming process using apt forming tools. Foster et al.^[25] investigated the influence of different quenching and cooling rates, respectively, on the final mechanical properties of AA6082. They used artificially aged conditions for comparison upon quenching/cooling directly in water, cooled flat tools and in air. Similar mechanical properties including yield strength (YS), ultimate tensile strength (UTS), and elongation to failure were found after quenching in water and the tool, whereas the air-cooled condition showed a significantly lower strength level.

In the novel thermomechanical process under consideration, the cooling of the heated blank is limited and controlled by the tool temperature. Forming with the help of heated tools prevents the preheated material from being subjected to high cooling rates as compared with cooled tools and, thus, leads to further improved formability. Therefore, several scientific studies already were conducted to establish a compromise between the cooling rate caused by different tool temperatures and maintenance of good formability. In these studies, the microstructural evolution and the mechanical behavior of the alloys under consideration were linked.^[26–31] Fan et al. and Yuan et al. investigated different forming processes using heated lower and upper tools as well as a gradient tool, i.e., a heated lower and a cooled upper forming tool. For this purpose, samples of heat treatable AA2A12 and AA6151 were investigated using a hat-shaped tool with a punch displacement of 40 mm at tool temperatures ranging from 100 to 350 °C. The aging treatment for both investigated materials was conducted at room temperature. To determine the mechanical properties, tensile samples were taken from the top side of the formed hat profile. As the temperature distribution of the preheated sheet during the positioning and forming is of a great importance in these experiments, the transfer time was kept as short as possible (3 s) and the forming time offset was set to 5 s. In their studies, the cooled upper and

heated lower forming tools configuration led to superior mechanical properties of the formed material at sufficiently good formability.^[29] Forming operations using a cooled upper tool allow for a high cooling rate and, thus, inhibit nucleation and growth of precipitations. As evidence, no coarse particles were observed in related conditions.^[28] Lower cooling rates imposed by heated tools promote precipitation already during the cooling step due to a sufficient level of diffusion.^[32]

The novel forming process in focus, as detailed earlier, promises a considerable improvement of forming limits and significantly reduced springback as compared with the state-of-the-art. At the same time, its potential to improve the mechanical properties of structural parts and to reduce processing times has been already revealed.^[30,33] For this reason, this technology is highly promising for serial production in the automotive sector and forming of lightweight, complex-shaped aluminum components.^[34] Considering this scenario, the parts used in the transportation industry, especially in crash relevant components, have to withstand a multitude of loading conditions, e.g., related to dynamic loading and energy absorption capability. Therefore, the dynamic plastic deformation behavior of the designed structures is of key importance. The relevant performance can be determined with the help of different techniques.^[35–37] Numerous studies already focused on the high strain rate (HSR) deformation behavior of aluminum alloys at room temperature.^[38–48] Yan et al. explored the strain rate sensitivity (SRS) of AA5059 aluminum alloy in a wide range of strain rates from 0.001 to 5000 s⁻¹.^[38] A positive SRS was observed up to 3500 s⁻¹, whereas SRS was found to be decreasing slightly with further increase in strain rate. Further investigations on the SRS of several aluminum alloys, focusing on the 6000 and 7000 series in the T6 condition, using Split-Hopkinson tension bar, were conducted by Chen et al.^[42] It was shown that plastic flow of the 6000 series at room temperature is less sensitive to the strain rate changes as compared with the 7000 series alloys. Concerning the dynamic deformation response of 7000 series alloys, an increase in YS and UTS as well as in total elongation was observed with increasing strain rate.^[49] The increase in these values during dynamic loading is reported in other studies as well.^[50–53] Other recent studies present models to rationalize and predict the evolution of microdefects based on the constitutive behavior for an AA5059 aluminum alloy to analyze hardening effects induced by thermally activated dislocation movement as well as flow softening at very high strain rates.^[54] The applied model shows high accuracy in predicting the stress response and evolution of voids for the investigated material. Of great interest, at least from the metal forming point of view, is the dynamic deformation behavior of formed parts after an integrated thermomechanical treatment. However, data reporting on the performance of differently processed aluminum alloys under impact loading and HSR deformation, respectively, are rare in open literature. Sasso et al. compared the high strain tensile deformation of AA7075 in T6 and O conditions using the Split-Hopkinson technique.^[55] Both conditions are characterized by an increase in yield and ultimate tensile strength with increasing strain rate. As expected, the strength reported for T6 was significantly higher than for the O condition. Furthermore, AA7075-O showed higher ductility and an increase in elongation at failure, respectively, at higher deformation rate, while the

elongation at failure of the T6 condition remained on the same level. In case of non-heat treatable aluminum alloys, e.g., the 5000 series, a decrease in flow stress with increasing strain rate in the range of 10^{-4} to 10^{-1} s^{-1} was observed, which then rises with increase of the strain rate up to $7.9 \times 10^2 \text{ s}^{-1}$.^[56] At very low strain rates, the flow behavior of this material at room temperature is characterized by the occurrence of serrations in the stress–strain curves.^[56–59] This occurrence is accompanied by the formation and propagation of shear bands on the sample surface, which are caused by the dynamic interaction between dislocations and mobile solute atoms.^[60–62] At very high strain rates, the stress–strain curve becomes smooth due to less-pronounced interaction between solute atoms and dislocations.^[56] This behavior was further found for aluminum alloy AA5083 as well as for Al–Mg alloys by Hopperstad et al. and Coë et al. focusing on investigations at 100 s^{-1} .^[63,64] At this point, however, it has to be noted that 6000 series and 7000 series alloys, at least in aged conditions, are by far less sensitive to these effects.^[65,66]

From analysis of current state-of-the-art, it becomes obvious that there is still a lack of data reporting on the characteristics of AA6082 and AA7075 alloys processed via the novel thermomechanical technique subjected to dynamic loading. As detailed earlier, many research works already focused on the behavior of thermomechanically processed high-strength aluminum alloys in the quasistatic regime. However, the characteristics of these alloys have to be explored in the HSR regime to understand in depth the relationships between mechanical properties and microstructural evolution of different conditions with respect to the envisaged fields of application. Thus, the aim of

this study is to investigate the HSR tensile behavior and at the same time, the local strain distribution evolution, of thermomechanically processed high strength aluminum alloys at different strain rates ranging from 40, 200, and 400 s^{-1} .

2. Experimental Section

2.1. Materials

In this study, two different heat treatable aluminum alloys were investigated: AA6082 (Al–Mg–Si), commonly used for structural components in automotive applications, and AA7075 (Al–Zn–Mg (–Cu)), which is typically favored in aerospace applications due to its high strength. The AR material condition (Table 1) of both alloys was T6 (solution heat treated, quenched, and artificially aged) being characterized by YS and UTS of 306 and 345 MPa for AA6082 and of 520 and 580 MPa for AA7075, respectively. Both materials were sectioned into blanks of $250 \times 180 \times 1.5 \text{ mm}^3$.

2.2. Forming and Heat Treatment Experiments

The hot forming process used in this work is schematically shown in Figure 1. Forming included three main steps: 1) solution annealing, 2) hot forming and quenching, and 3) artificial aging. All steps were in line with the procedure detailed for the novel thermomechanical process recently introduced in the studies by El Fakir et al. and Mohamed et al.^[22,67] The integrated forming process combines hot forming and quenching of the heated blank within the forming tools after initial SHT. In this regard, initial SHT is conducted to homogeneously dissolve the alloying elements within the Al matrix. The subsequent forming operation allows for both realization of complex-shaped geometries enabled by hot forming and realization of a supersaturated solid solution (SSSS) state due to the high cooling rate imposed by forming. Eventually, the cooling rate can be tailored by adequate tool temperature. Subsequently, the hardenable material is artificially aged

Table 1. Chemical composition of the investigated alloys determined by optical emission spectroscopy.

Chemical elements [wt%]	Si	Fe	Cu	Mn	Mg	Cr	Zn	Ti	Others
1 AA6082—AR	0.9	0.42	0.10	0.44	0.8	0.02	0.19	0.04	0.03
2 AA7075—AR	0.08	0.12	1.6	0.04	2.7	0.19	5.9	0.05	0.03

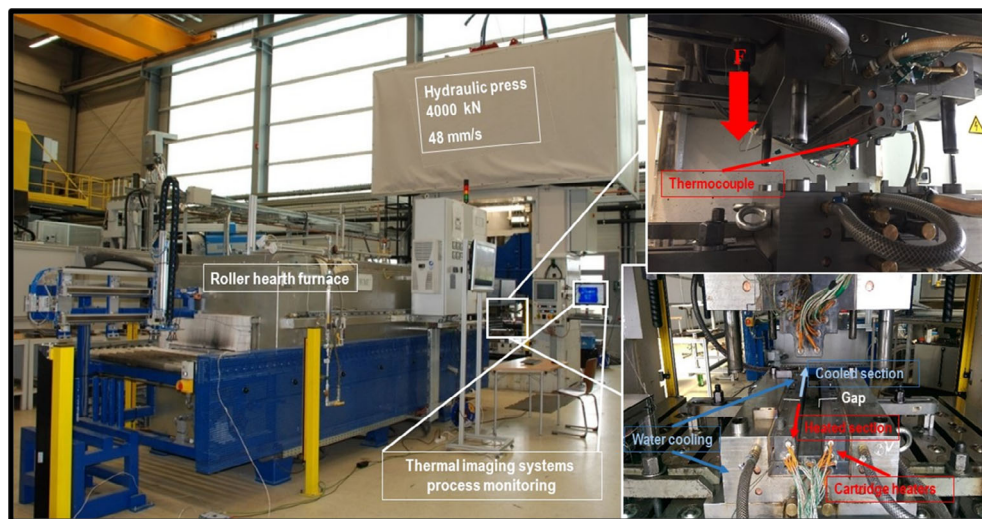


Figure 1. Illustration of the thermomechanical process route used (left) including detailed views on the tempered forming tools (right). See main text for details.

Table 2. Main experimental parameters used in this work.

	Investigated material	SHT temperature [°C]	SHT time [s]	Tool temperature [°C]	Aging
1	AA6082—AR AA7075—AR	—	—	—	—
2	AA6082 AA7075	540 480	900 900	24 24	165 °C—8 h 120 °C—20 h
3	AA6082 AA7075	540 480	900 900	200 200	165 °C—8 h 120 °C—20 h
4	AA6082 AA7075	540 480	900 900	350 350	165 °C—8 h 120 °C—20 h

to obtain full strength and enhance the mechanical properties. The thermomechanical process parameters detailed in **Table 2** focused on the influence of different cooling rates on the final mechanical properties of both alloys. Accordingly, the sheet materials were first heated up to 540 °C in case of AA6082 and 480 °C in case of AA7075 (as recommended in literature to avoid overheating^[30,33]) in a roller hearth furnace and soaked for 900 s at the SHT temperature. After the transfer, taking around 6–8 s, the heated blanks were formed and quenched either within cooled (24 °C) or heated forming tools (200, 350 °C) for 30 s. Rapid cooling aimed at suppressing the nucleation of precipitations and establishing a metastable, supersaturated state. Heated tools were used to decrease the cooling rate during the forming process and eventually allow for the evolution of precipitates and their

respective growth already at this stage. All formed blanks were aged immediately at 165 °C for 8 h in case of AA6082 and at 120 °C for 20 h in case of AA7075, respectively, to obtain a well defined condition on further cooling to room temperature. The aging parameters used in this work have been selected based on own previous investigations^[13,30] and aimed at obtaining similar mechanical properties, with a primary focus on superior strength, similar to commercial T6 condition. Obviously, maximum achievable strength in the conditions formed at a tool temperature of 350 °C is lower due to loss of solutes imposed by less efficient quenching. Still, aging parameters used lead to highest strength being achievable in this condition. Furthermore, the conditions obtained upon artificial aging treatment did not suffer any further changes in precipitate characteristics during storage and testing at ambient temperature and, thus, are referred to as “stable conditions” in the remainder of the article (even if not being in a thermodynamically stable condition). These states were then the base conditions for further investigations.

2.3. Property Characterization and Test Setup

To characterize the prevailing microstructures of the formed parts after thermomechanical processing and the deformation properties under dynamic loading conditions, the testing procedure, as schematically shown in **Figure 2**, was designed. Tests were conducted for all conditions established (forming tool temperatures of 24, 200, 350 °C) and results obtained compared with the AR T6 condition. Detailed information on the individual is provided in the following subsections.

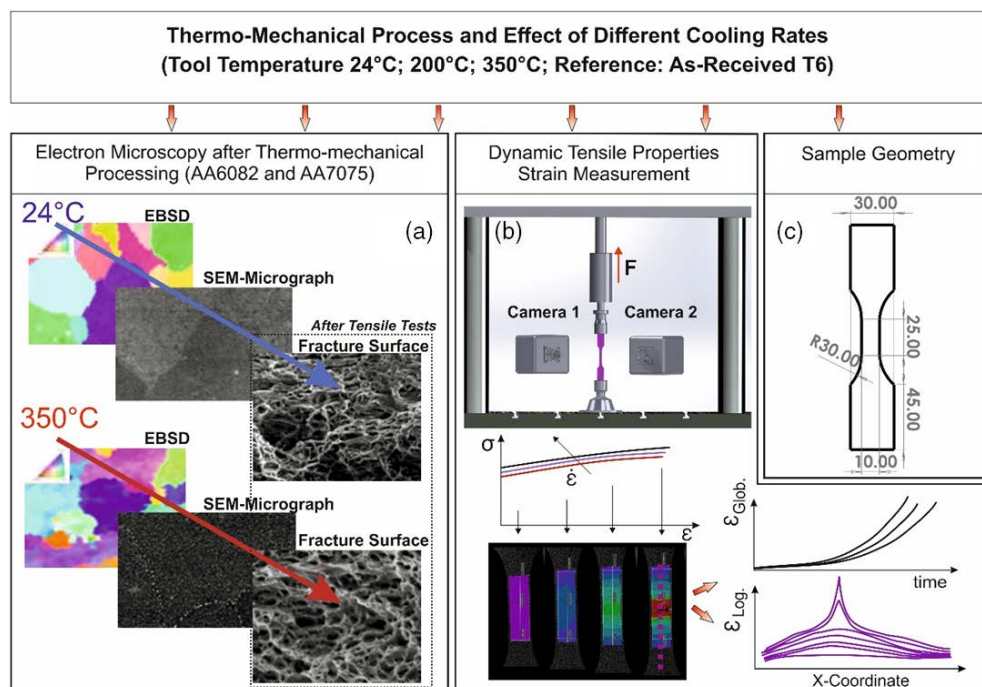


Figure 2. Schematic illustration of the experimental procedure upon thermomechanical treatment. a) Microstructural characterization using EBSD technique and BSE imaging as well as fractography, b) HSR tensile testing including non-contact full field 3D strain measurement, and c) sample geometry (thickness $t = 1.5$ mm).

2.3.1. Tensile Tests

The samples for tensile testing were machined by electrical discharge machining with a gauge length and width of 25 and 10 mm, respectively, Figure 2c. Samples for all strain rates were sectioned along the rolling direction of the formed parts in the condition after the aging process. A servohydraulic high-speed tensile testing machine (HTM8020, Zwick and Roell GmbH & Co. KG) equipped with an 80 kN load cell (effective piston stroke of 250 mm and maximal piston speed of 20 m s^{-1}) was used to determine the properties of the formed parts under dynamic tensile loading. All tensile tests were conducted at room temperature and at three different nominal strain rates, i.e., 40, 200, and 400 s^{-1} . Three tensile tests for each condition were conducted for both materials. During the tests, the kinetic energy of the initially accelerated piston is transformed into deformation work eventually causing the dynamic plastic deformation of the fixed specimen inside the machine, Figure 2b. This effect leads to an oscillation of the whole testing rig, which is most pronounced at highest deformation speeds. As a result, the obtained tensile curves, especially for the tests at higher strain rates, are characterized by serrated flow and wavy propagation. It is important to note that this behavior is not related to the intrinsic mechanical behavior of the tested material. This kind of wavy behavior has been already reported and discussed for tests at very high strain rates for various alloys in literature.^[43,68–70]

2.3.2. Digital Image Correlation

To characterize the local strain evolution in the investigated samples, the digital image correlation (DIC) technique (the setup for acquiring optical images being coupled with the tensile testing machine) was used for tests at all strain rates. To guarantee for adequate contrast on the sample surface, a surface pattern was applied using two different colors sprayed onto the

surface.^[71,72] The local strain measurement was conducted based on data recorded by two high-speed cameras (Photron Europe limited fastcam-X2) in stereographic arrangement focusing on the tensile specimen surface. The used high-speed cameras are equipped with high-performance objective lenses Rodagon 80 (focal length of 80 mm and image circle of 65 mm). The resolution for all experiments was set to 384×264 pixels and the frame rate at 100 Kfps. Data were evaluated using commercial software for calculation of full-field 3D strain maps (VIC-3D, Correlated Solutions).

2.3.3. Microscopy

A scanning electron microscope (SEM) equipped with an electron backscatter diffraction (EBSD) unit operating at a nominal voltage of 20 kV was used to characterize the microstructure and fracture surfaces of the samples in various conditions. Standard grinding and polishing procedures were used for sample preparation. For EBSD measurements, the samples were prepared by additional 24 h of vibropolishing in a colloidal silica solution (OPS). The step size of EBSD measurements used for all conditions was $1.5 \mu\text{m}$. Grain sizes were determined by both the linear intercept method and the EBSD OIM software.

3. Results and Discussion

3.1. Microstructure Investigation

3.1.1. EBSD

The effects of thermomechanical processing on the grain sizes and general microstructure appearance of AA6082 and AA7075 alloys were analyzed by EBSD measurements. **Figure 3** shows the EBSD images (inverse pole figure [IPF] maps) of both aluminum alloys in different conditions. Grain sizes of AA6082

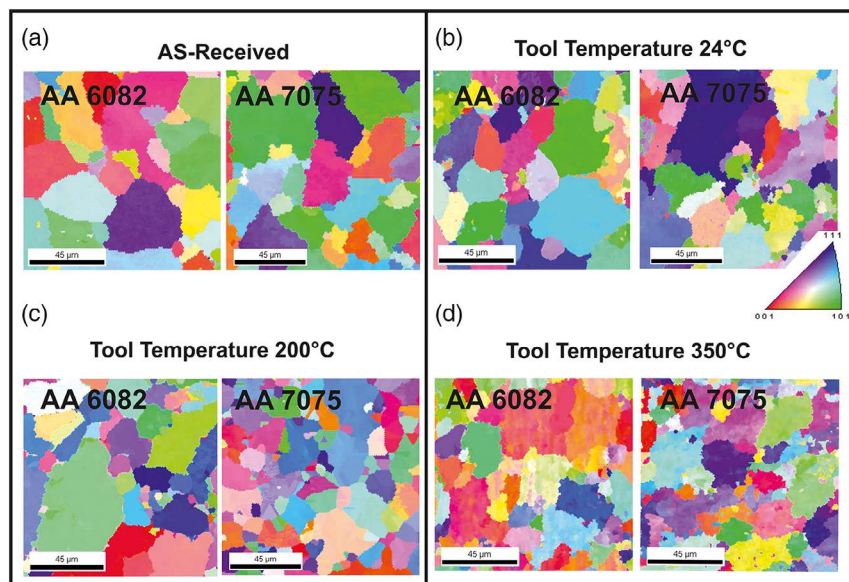


Figure 3. EBSD micrographs (IPF maps) for a) AR conditions and samples formed in the tool with temperatures of b) 24°C , c) 200°C , and d) 350°C . Color coding is plotted for RD according to the standard triangle shown on the upper right of (b); See text for details.

and AA7075 alloys in the AR condition were determined to be 32 and 25 μm , respectively. Generally, the combination of solution heat treatment and hot forming at various tool temperatures only leads to minor differences in the grain sizes of both alloys although the microstructures of the samples formed in the hot tools show the development of substructures. The grain sizes of AA6082 and AA7075 alloys after thermomechanical processing in tools with various temperatures were determined to be in the range of 27–29 and 22–25 μm , respectively. Previous investigations on these alloys also revealed the constancy of grain sizes during hot stamping.^[34,73] Solute elements are thought to be responsible for inhibiting recrystallization and subsequent grain growth by reducing grain boundary mobility.^[74]

3.1.2. Backscattered Electron Contrast Analysis

The microstructures of both alloys formed and quenched/cooled in the tools with different temperatures were further analyzed by SEM utilizing backscattered electron (BSE) contrast, as shown in **Figure 4**. From these micrographs, it can be deduced that the tool temperature is a very influential parameter on the sizes and morphologies of precipitates formed in the subsequent aging treatment. Coarse precipitates are seen in case of the samples of both alloys formed and cooled within the hot tools (350 °C), while very fine and dispersed precipitates were formed in those conditions quenched in the cold tools (24 °C). Such fine and dispersed precipitates are known to significantly enhance the strength of metallic materials due to the interaction between these second-phase particles and dislocations.^[75,76] Improved strength of both

alloys formed and quenched in the cold tool can be ascribed to the formation of fine and well dispersed precipitates throughout the microstructure. In case of the AA7075 sample formed and cooled in the hot tool, microstructure consists of fine precipitates in the grain interior and relatively coarse precipitates along the grain boundaries, **Figure 4d**. Lower cooling rate after solution treatment leads to the development of relatively large precipitates along the grain boundaries, eventually causing a depletion of the surrounding areas in precipitate forming elements.^[77,78] Therefore, formed precipitates during subsequent aging treatment are not adequate for strengthening of the material. Further analysis of microstructure evolution on a lower scale is currently under consideration and will be published in follow-up studies, as these studies are clearly beyond the scope of this work.

3.2. Effect of Cooling Rate on HSR Tensile Deformation

The quasistatic tensile behavior of AA6082 and AA7075 has already been reported in previous studies.^[30] For brevity, data are not shown here. Previous results revealed that higher forming tool temperatures result in lower strength, however, higher elongation at failure for both alloys. In **Figure 5**, the true stress–true strain behavior of AA6082 upon processing at forming tool temperatures of 24, 200, and 350 °C as well as in the AR condition (T6) is shown for the three strain rates of 40, 200, and 400 s^{-1} . The evolution of plastic strain of the studied conditions was determined using the DIC system coupled with data obtained by the load cell of the test machine. The results reveal no significant change in YS and UTS for the AR and hot formed conditions for tool temperatures below 200 °C. Upon increase in

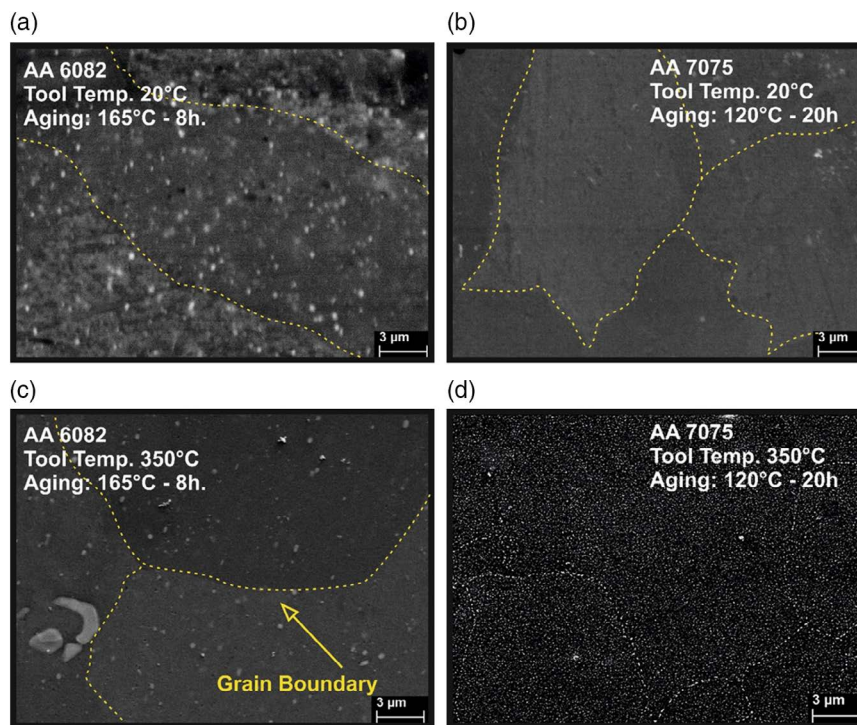


Figure 4. BSE micrographs of samples manufactured in tools with temperatures of a,b) 24 °C and c,d) 350 °C (The pictures on the left and right show AA6082 and AA7075 alloys, respectively). See text for details.

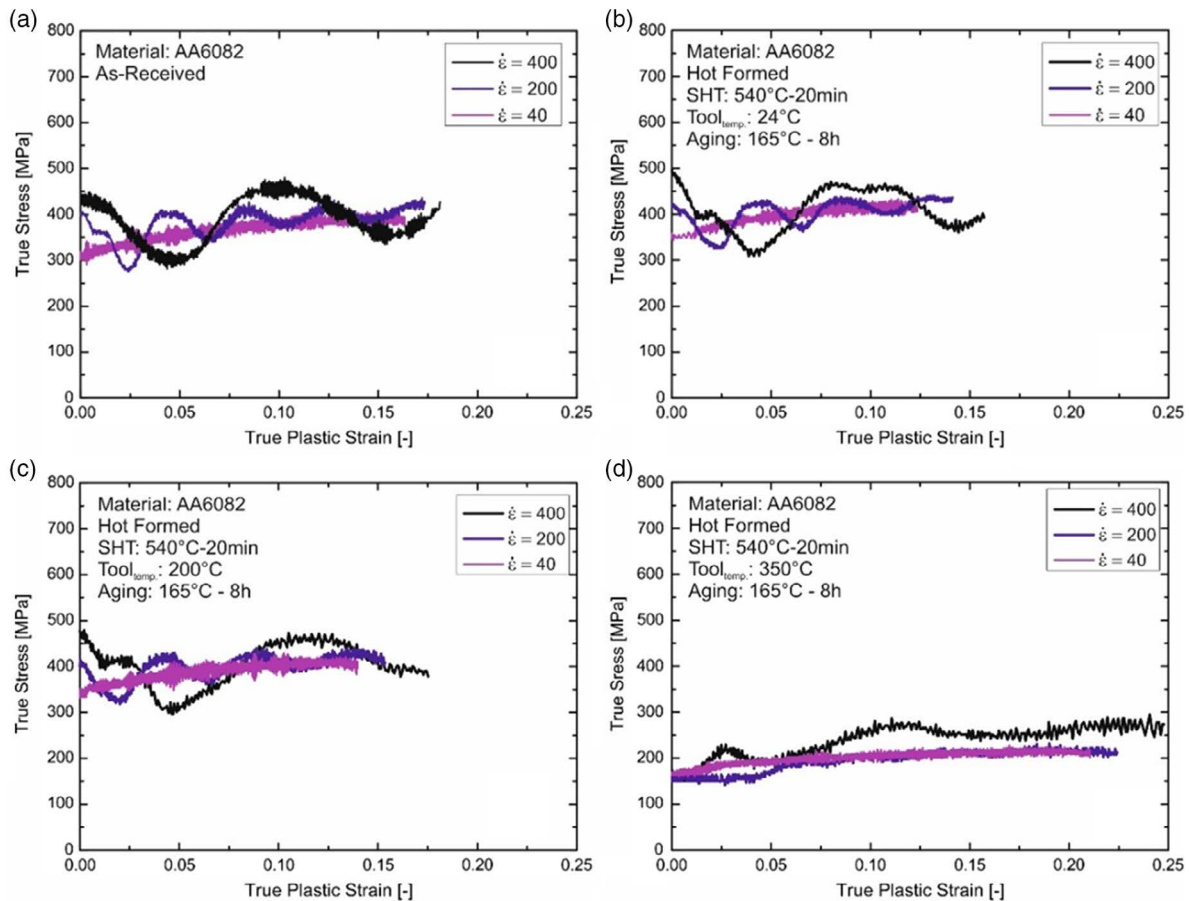


Figure 5. Dynamic tensile behavior of AA6082 in a) AR condition and upon forming at tool temperatures of b) 24 °C, c) 200 °C, and d) 350 °C for three different strain rates (40, 200, and 400 s⁻¹).

the tool temperature to 350 °C, UTS of the material decreases significantly from 480 to 277 MPa. Focusing on plastic deformation, the material hot formed at 350 °C tool temperature is characterized by a pronounced increase in elongation at failure to $\epsilon_{\text{true}} = 0.25$. These observations can be rationalized based on the cooling conditions, where nucleation of precipitates and the segregation of alloying elements at grain boundaries are promoted. Furthermore, by comparing the flow behavior of all conditions, the curves of the 350 °C condition appear to be less sensitive to the rate of deformation. This specific behavior changes at higher strain level and a slight increase can be observed, however, only for the highest strain rate (400 s⁻¹). Clearly, upon increasing the strain rate up to 400 s⁻¹, an increase in YS, UTS and elongation at failure is evident for all conditions. It has to be noted that the mechanical properties of the materials formed at 24 and 200 °C tool temperature are absolutely similar to those of the AR material.

Figure 6a–d show the dynamic deformation responses of AA7075 at different strain rates (40, 200, and 400 s⁻¹) after thermomechanical processing. The trends already detailed for AA6082 can also be deduced for this material. Forming and cooling at a very high tool temperature, e.g., 350 °C, results in a severe decrease in YS and UTS as compared with conditions formed at lower tool temperatures, **Figure 6b,c**. In contrast to

the dynamic behavior seen in case of AA6082, however, no strong increase in elongation at failure is seen for AA7075 in the 350 °C condition. Thus, this specific condition of AA7075 generally is less sensitive to strain rate changes as compared with the companion AA6082 condition. However, considering all thermomechanical processed conditions and the AR material of the AA7075, a significant increase in YS, and only minor effects on UTS as well as plastic elongation are seen when the strain rate increases. Similar trends are seen for all conditions considered (AA6082 and AA7075), except the hot stamped materials in the 350 °C condition.

In general, the strength of solid metals is related to their resistance against plastic deformation. Hence, the main mechanisms governing the strength of hardenable face-centered cubic (FCC) aluminum alloys (also at high strain rates) can basically be linked to dislocation–dislocation interaction as well as complex dislocation–precipitate interaction. However, it is well established that the contributions of single elementary mechanisms related to macroscopic and microscopic deformation change at higher strain rates as compared with the quasistatic regime. For FCC materials, it is reported that higher strain rates during plastic deformation lead to a pronounced increase in the dislocation density due to the activated cross-slip mechanism.^[79–82] Due to the higher dislocation density mutual pinning significantly contributes to an

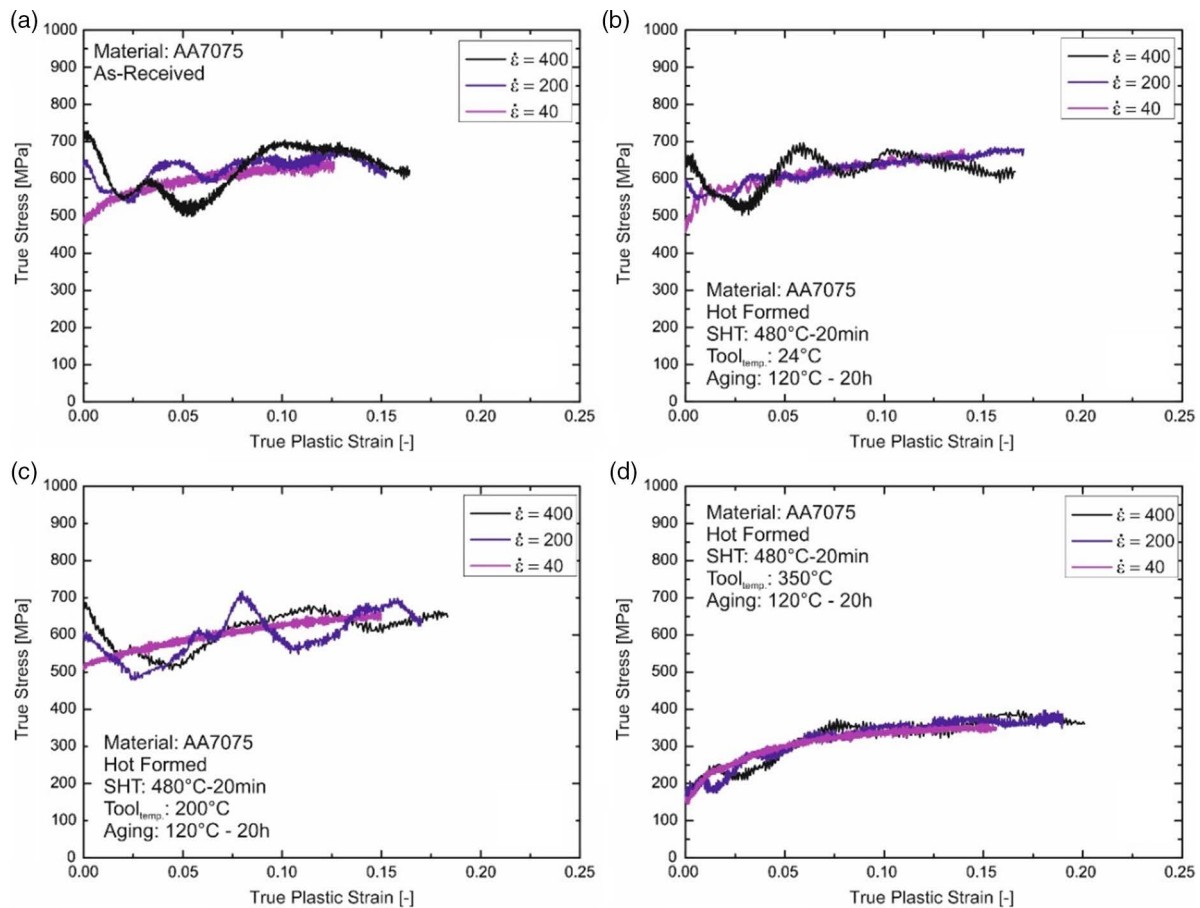


Figure 6. Dynamic tensile behavior of AA7075 in a) AR condition and upon forming at tool temperatures of b) 24 °C, c) 200 °C, and d) 350 °C for three different strain rates (40, 200, and 400 s⁻¹).

increase in strength. In this regard, the mechanism being primarily responsible for an increase of strength of the FCC material at very high strain rates is thought to be based on their crystal structure and the intrinsic behavior and interaction of lattice defects. The material response to strain rate and temperature at extremely high deformation rate was investigated using atomistic simulation to reveal the governing mechanism most efficiently contributing to material strength.^[83] It was reported in several studies that up to a strain rate of $\dot{\epsilon} = 10^8$ s⁻¹ work hardening and thermal activation mainly contribute to material strength.^[84,85] At extremely high levels, however, this situation changed in the favor of phonon drag. In case of the FCC material studied by Yaghoobi and Voyiadjis, it was approved that work hardening due to pronounced dislocation interaction is the governing mechanism over a wide range of strain rates, whereas the contribution of thermal activation mechanisms were assumed to be insignificant.^[83] In this regard, strain rates considered in this work are obviously in a regime that is dominated by dislocation interaction.

However, the most important feature providing for effective strengthening of aluminum alloys is the presence of nanoscopic second-phase particles, which act as obstacles for dislocation motion.^[86] The in-depth analysis of dislocation-defect interaction is a very challenging task, becoming even more complex at high strain rates.^[87] Atomistic simulations conducted on

precipitation hardenable alloys have shown that the dislocation mobility is highly sensitive to the type of precipitates and their morphology. Large-scale discrete dislocation dynamic (DDD) simulations focusing on the interaction between dislocations and small (and strong) precipitates have revealed the presence of serrated dislocations at high strain rates due to the pinning effect related to the immovable precipitates.^[87] This fact enables different geometrical options to overcome misfit obstacles based on several elementary mechanisms eventually leading to distinctly different behavior of moving dislocation. In this regard, both the position and location of the dislocations play a relevant role.^[88] During these complex interaction processes, dislocation loops can form in front of and behind the existing particles in the matrix. Eventually, these phenomena lead to a very complex microstructure evolution including interactions between loops and straight dislocations in addition to dislocation-precipitation interaction resulting in higher shear stresses.

It was further concluded that the related SRS depends strongly on the number of obstacles.^[89-93] Applied stress as well as the particle nature and size are the key elements controlling the thermally affected dislocation motion, i.e., affecting SRS at high strain rates.^[91]

It is expected that the unzipping phenomenon of a mobile dislocation primarily is connected to passing of weak obstacles.

By changing the particle geometry, number, distance, and applied shear stress, dislocation shape and motion are expected to change fundamentally. Under this condition, it was shown that the SRS is more pronounced when the particles are weaker, i.e., less effective.^[91,94] Due to the prevalent interaction mechanism, relatively fine and randomly distributed obstacles were shown to lead to pronounced SRS and higher flow stress.^[95] All these aforementioned factors are thought to be an explanation for the high SRS for both materials in T6, 24 and 200 °C conditions, where fine distribution of precipitates is a major characteristic. It should, however, be also noted that very high values of strain rates were considered in the aforementioned studies,^[79–81,86,89,93–97] whereas the values of strain rates in this work are not as high such that only qualitative assertions can be made.

3.3. Effect of Cooling Rate on Local Deformation Behavior at Different Strain Rates

The local deformation behavior of all thermomechanically processed conditions of AA6082 for all strain rates considered is shown in **Figure 7** by highlighting the progression of the logarithmic strain distribution up to failure (evaluated for the tensile direction). For the AR condition, a homogenous plastic strain distribution is seen before necking appears. After necking and before final failure, respectively, strain localization is a characteristic feature at all strain rates. With increasing the strain rate up to 400 s⁻¹, neck initiation appears at higher global strain, according to the strain determined based on DIC data. Interestingly, the absolute level of logarithmic strain within the failure region of the AR material remains on the same level for all strain rates ($\epsilon_{\text{Log}} = 0.43$), **Figure 7a–c**. The logarithmic strain evolution for the 24 and 200 °C tool temperature hot-formed materials are shown in **Figure 7d–i**. Qualitatively almost the same behavior is seen as in case of the AR material, i.e., a homogenous plastic deformation distribution at the very early stages of deformation before necking. As plastic deformation proceeds, however, necking appears for both conditions at a lower global strain level. Referring to the stress–strain behavior of these conditions, **Figure 5**, slightly higher deformation at failure is seen for the AR material as well. Therefore, based on the observations made by DIC and tensile tests, it can be deduced that hot forming at 24 and 200 °C tool temperatures affects both strain localization and neck propagation of the material during plastic deformation.

Dynamic tensile tests after hot forming within the tempered forming tools at 350 °C reveal a pronounced increase of ductility of the material. At the same time, local strains along the gauge length of this condition determined by DIC measurements reveal higher absolute values as compared with other conditions, **Figure 7j–l**. In addition, the necking point appears at higher global strains and a continuous increase in global elongation concomitant to a high degree of strain localization evolving up to failure is seen. The logarithmic strain determined at the highest strain rate of 400 s⁻¹ shortly before failure is $\epsilon_{\text{Log}} = 0.55$.

The local deformation behavior of AA7075 at high strain rates (40, 200, and 400 s⁻¹) along the gauge length of the tensile specimen for all conditions is shown in **Figure 8**. A homogenous plastic deformation and a qualitatively similar behavior as for AA6082 can be deduced for AA7075 along the gauge length of the sample. In

the early stages of deformation, a homogenous strain distribution is seen up to the necking point. Upon increasing the plastic deformation to higher levels, strain localization appears, which is more pronounced for the AR material. This phenomenon can be clearly seen by comparing the necking width (NW) in **Figure 8c,f**, where a narrow necking band is resolved by DIC for the AR condition. However, the obtained strain level ($\epsilon_{\text{Log}} = 0.35$) for this alloy is much lower as compared with AA6082 ($\epsilon_{\text{Log}} = 0.43$) at the highest strain rate. Hot-formed material (at forming tool temperature of 350 °C) shows higher logarithmic strains up to $\epsilon_{\text{Log}} = 0.40$. Considering all the thermomechanically treated samples, a higher logarithmic strain (in terms of the local maximum strain related to the neck) is obtained with increasing strain rate for both AA6082 and AA7075. One further phenomenon that should be considered at very high strain rates for both materials is adiabatic heating.^[57] Its occurrence counteracts the work hardening during dynamic plastic deformation and leads to softening of the material as well as to strain localization, as shown for AA6082-T6 by Chen et al. and Ashuach et al. based on investigations at 3400 and 5000 s⁻¹, respectively.^[47,70] The strain rates considered in present work are significantly lower as compared with those studies, where a detailed investigation of adiabatic heating was conducted.^[42,70] In light of these considerations, the influence of adiabatic heating for the investigated materials can be neglected as indirectly revealed by work hardening, i.e., an increase in material strength is seen at increasing strain rate.

From the DIC results presented, it can be deduced that a high deformation rate leads to a delay in the appearance of strain localization and eventually necking. This behavior is clearly shown in **Figure 8g–i**, where necking, i.e., a strongly localized increase in strain level, at a lower global true plastic strain level for the lower strain rate as compared with the higher strain rate is seen. Hence, at higher strain rate, the distribution of plastic strains is more homogeneous as early necking is impeded and, thus, the overall global strain value of the material at failure increases. The significant increase in local and global strains seen for the hot-formed material at a tool temperature of 350 °C can be rationalized based on the material condition induced by the low cooling rate during hot forming leading to the evolution of coarse particles and their only moderate contribution to strengthening. Further, interesting observations based on the tests conducted at 400 s⁻¹ focusing on the logarithmic strain distribution are shown in **Figure 7f** and **8i**, where apparently two strain peaks at different locations on the sample surface appear. Obviously, this behavior is not limited to only one material and was observed for both AA6082 and AA7075. However, in case of these two materials such behavior was found for different material conditions in this work, i.e., AA6082 formed at a tool temperature of 24 °C (**Figure 7f**) and AA7075 formed at a tool temperature of 200 °C (**Figure 8i**). The observed peaks can be regarded as neck nucleation regions. However, only one of the two neck initiation regions dominates thereafter and eventually leads to failure. This behavior can be most clearly seen in case of AA7075 hot stamped at a tool temperature of 200 °C in direct comparison with the reference condition shown, **Figure 8i** and **9b** versus **Figure 8c** and **9a**. The observation of multiple neck initiation points for the investigated material at high strain rates is thought to be affected by minor fluctuations in terms of plastic flow stability and, thus, slightly accelerated local deformation in distinct

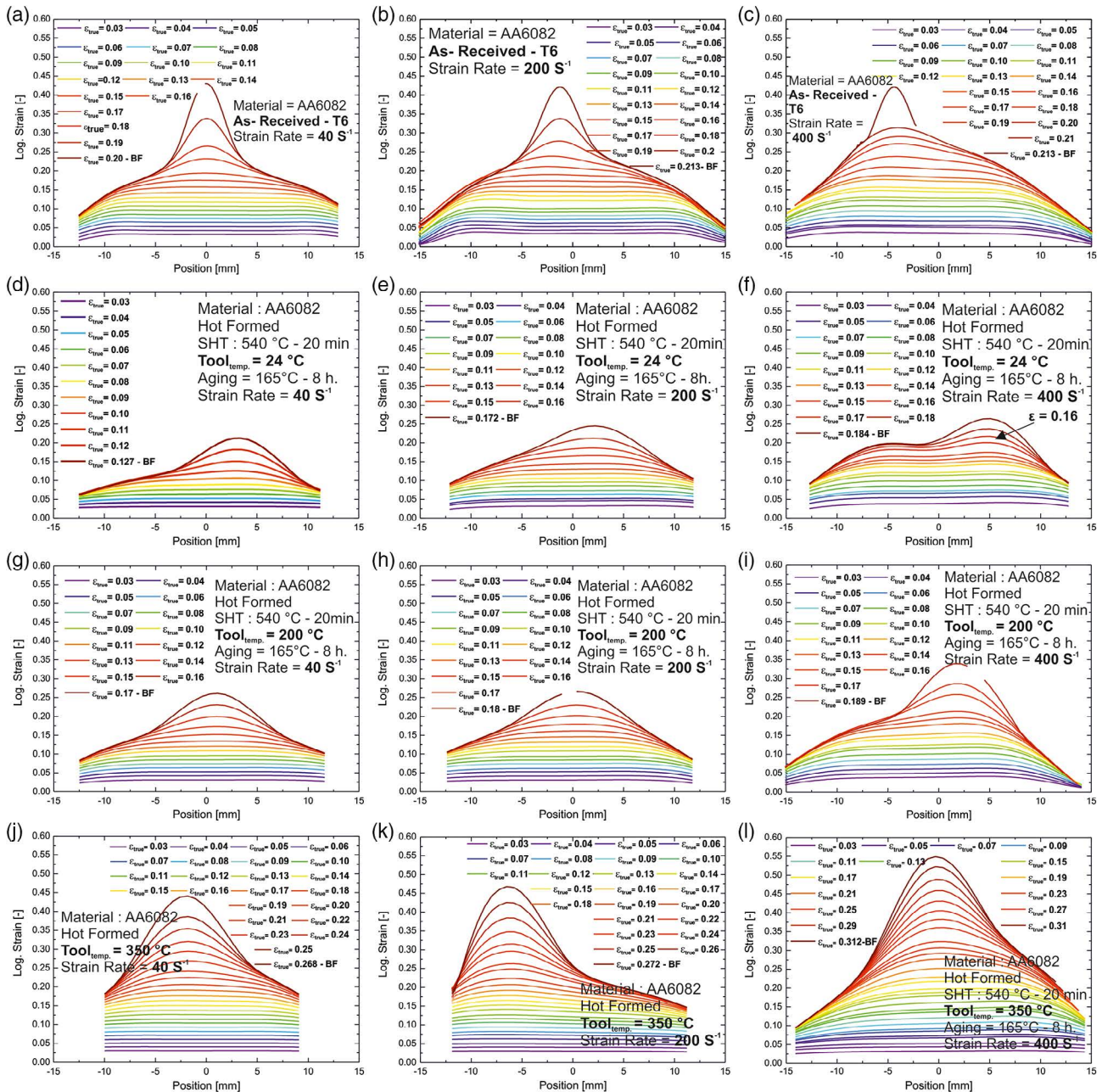


Figure 7. Local deformation distribution determined by DIC for AA6082 samples at different levels of global strain in a–c) for the AR condition, d–f) the condition formed at tool temperature of 24 °C, g–i) the condition formed at tool temperature of 200 °C, and j–l) the condition formed at tool temperature of 350 °C.

regions.^[98–101] The phenomenon of initiation of multiple necking sites during dynamic loading using a hemisphere expansion setup coupled with an ultra-high speed camera focusing on pure copper and tantalum has been shown by Mercier et al.^[98,102] For both materials, multiple necking sites initiated alongside meridians at high plastic deformation levels due to flow instability at these high strain rates. Moreover, based on the developed theoretical model in that study, a SRS parameter was defined, eventually combining the effects of strain hardening, thermal

softening, and SRS. It was assumed that the onset of multiple necking appears when this parameter reaches the saturation level. In this regard, the saturation level strongly depends on the material parameters, e.g., SRS. Multiple necking formation and growth in pure aluminum at very high strain rates was also observed in an investigation performed using a Split-Hopkinson Pressure Bar setup by Besnard et al.^[103] In that study, the 3D strain distribution on the sample surface was experimentally determined using high-speed cameras through a stereovision

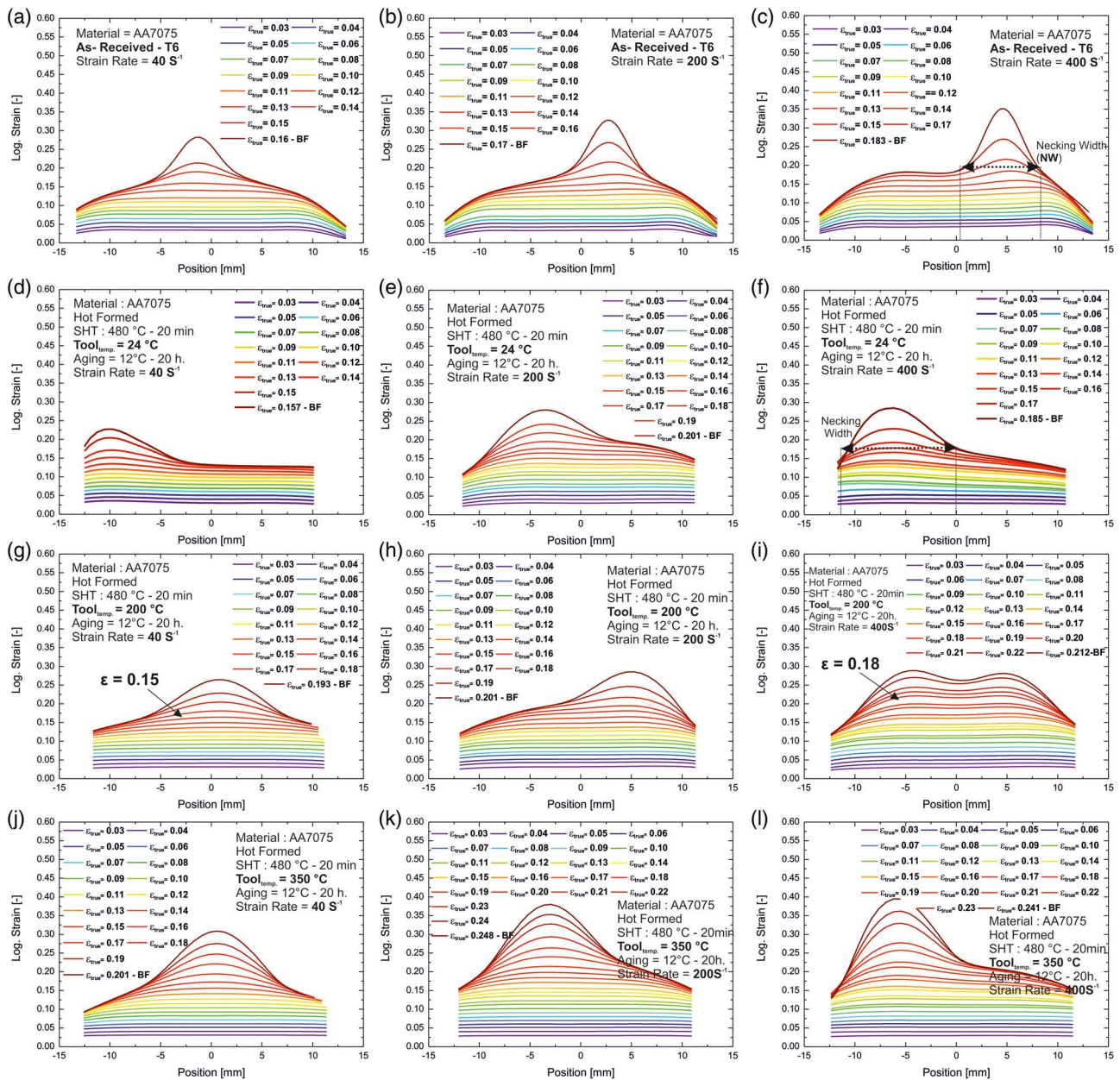


Figure 8. Local deformation distribution determined by DIC for AA7075 samples at different levels of global strain in a–c) for the AR condition, d–f) the condition formed at tool temperature of 24 °C, g–i) the condition formed at tool temperature of 200 °C, and j–l) the condition formed at tool temperature of 350 °C.

setup. Based on results shown, it was discussed that the simultaneous growth of two necks in pure aluminum is caused by the competition between neck initiation in multiple sites and the growth of a few dominant necks. Mutual interaction of these necks has been described by the Mott model.^[104] In this regard, complex deformation phenomena on the submicron scale lead to significant effects on the macroscopic level being evaluated in this study using the DIC technique. In-depth analysis of the relevant elementary mechanisms on the micrometer and submicrometer scale, however, is clearly beyond the scope of this study and, thus, will be subject of follow-up work.

3.4. Fractography

To further analyze the failure mechanisms of AA6082 and AA7075 alloys after dynamic tensile tests, the fracture surfaces were investigated. Typical dimple-like facets and microvoids are evident on the fracture surfaces of all AA6082 alloy samples after dynamic tensile testing (Figure 10). Existence of large and deep dimples reveals that most pronounced ductile failure occurred during high strain tensile tests as also reported in previous studies for another aluminum alloy.^[105] As discussed earlier, considering the strain rate range of present work in

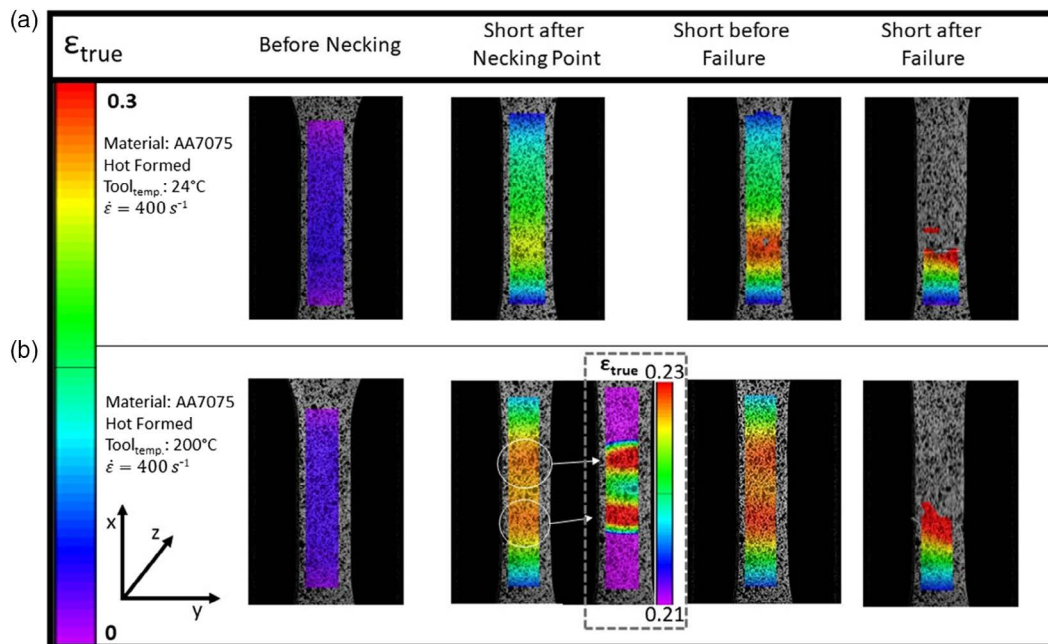


Figure 9. Local deformation maps for AA7075 deformed at 400 s^{-1} after hot stamping at a) $24 \text{ }^\circ\text{C}$ and b) $200 \text{ }^\circ\text{C}$. True strains are plotted with respect to the loading direction. The absolute true strain values are represented by the scale bar depicted on the left. See text for details.

comparison with data available in literature, adiabatic heating is thought to be not effective here. Upon direct comparison of fracture surfaces, larger and deeper dimples can be seen in case of the samples formed in the hot tools (Figure 10e,f), eventually confirming higher ductility of the respective conditions in the examined strain rate regime.

Fracture surfaces of the AA7075 alloy deformed at high strain rates are shown in Figure 11. Comparing the fracture morphologies of both alloys, the dimples are larger and deeper in case of the AA6082 alloy in all conditions. These observations can be rationalized in terms of the generally higher ductility of the AA6082 alloy as compared with that of AA7075. Also for the AA7075 alloy, dimples being seen for samples formed and cooled in the hot tool are significantly larger in terms of size and depth (Figure 11e,f) as compared with the other AA7075 conditions (Figure 11a–d). The effect of strain rate on the appearance of fracture surface morphologies of the samples tested under dynamic tensile loading conditions is not significant, however, fracture surfaces of samples tested at higher strain rates seem to show a higher fraction of ductile fracture facets in comparison with those tested at lower rates. Same fracture morphologies were already reported after HSR tensile testing of Al–4.8Cu–1.2Mg alloy.^[105]

Theoretically, dimple and shear fractures are the two main features, however, their appearance depends on the actual stress state. Most important in this regard is the growth mechanism of the voids in the HSR regime.^[106] At dynamic tensile deformation, competition between strain hardening and thermal softening can affect the fracture morphology of materials.^[105] Shallow dimples form where strain hardening is dominant, while large and deep dimples and shear bands are expected in case of dominance of thermal softening. Very high values of strain rates explored in the aforementioned studies^[105,106] result in

noticeable thermal softening due to adiabatic heating. In the present study, local increase in temperature is expected not to be that pronounced to the significantly lower strain rates considered. However, still localized effects are thought to lead to the formation of relatively larger and deeper dimples at higher strain rates (cf. Figure 10 and 11).

4. Process–Microstructure–Property Relationships

To summarize present findings and to establish solid process–microstructure–property relationships, the influence of the process route on the microstructural development and the dynamic tensile deformation behavior of the studied age-hardenable aluminum alloys are discussed in an integrated fashion in this section. Relevant relationships are shown and highlighted schematically in Figure 12. The microstructural evolution of AA6082 and AA7075 alloys upon various thermomechanical processing steps is schematically shown in the lower half of Figure 12. First, the AR T6 condition is heated up to the SHT temperature and soaked to dissolve existent precipitates. Then, hot forming and quenching in tools with different temperatures and subsequent aging treatment result in the evolution of dislocations and precipitates in the microstructure of both alloys. However, forming and quenching conditions significantly affect the microstructure. As schematically illustrated, low cooling rates lead to instantaneous precipitation and further promote the evolution of grain boundary segregations within the following aging step. Concomitantly, elevated temperatures allow for relaxation and recovery and, thus, the dislocation density in this condition is relatively low. On the contrary, higher cooling rates imposed by cold tools allow to maintain the supersaturated state such that only during the subsequent aging treatment the formation of

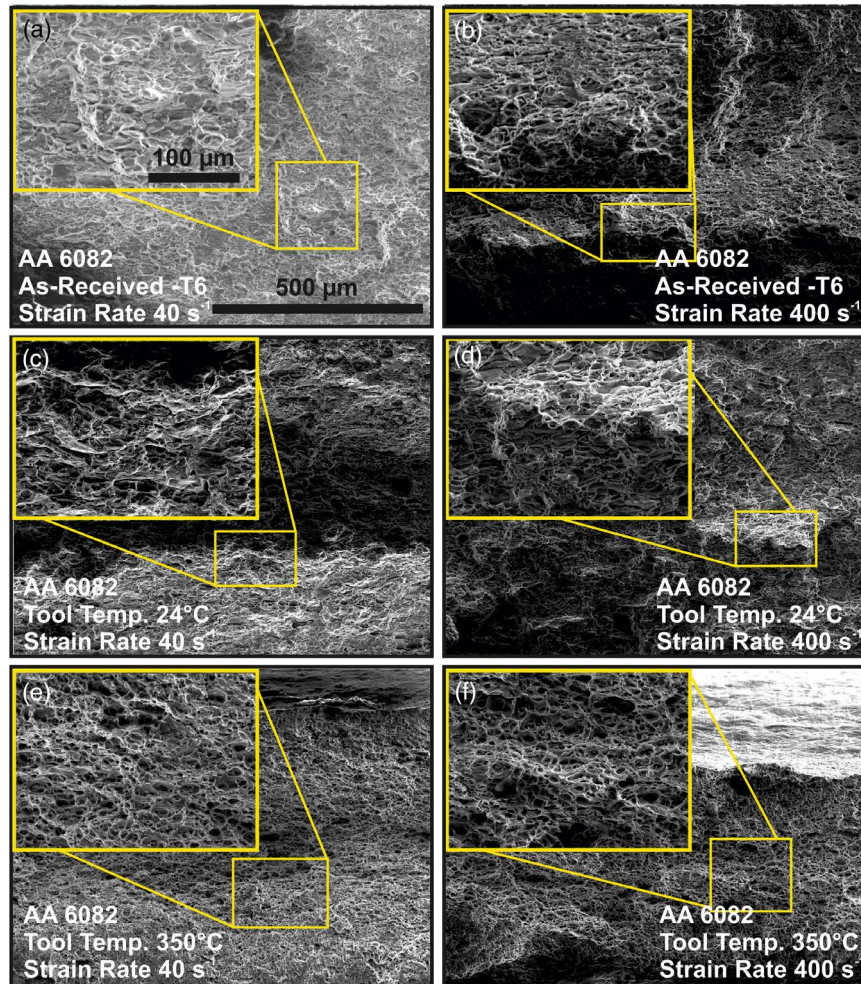


Figure 10. Fracture surfaces of AA6082 alloy in AR condition tested at a strain rate of a) 40 s^{-1} , b) 400 s^{-1} ; fracture surfaces of sample formed in the tempered tools at temperatures of c,d) $24 \text{ }^\circ\text{C}$ and e,f) $350 \text{ }^\circ\text{C}$. Samples were tested at a strain rate of c,e) 40 s^{-1} and d,f) 400 s^{-1} (Pictures and insets show low and high magnifications, respectively.)

precipitates is promoted, eventually leading to finer and randomly distributed precipitates.^[78] At the same time, forming in cold tools impedes relaxation and recovery such that upon forming a medium dislocation density prevails.

During deformation, for large and coarse precipitates, two different kinds of dislocation-precipitate interaction prevail. Bowing, looping, and by pass, respectively, of moving dislocations is the relevant mechanism in case of coarse precipitates. On the contrary, in case of the small precipitates cutting is the relevant mechanism. Furthermore, distances between precipitates are significantly different as the overall volume fraction of precipitates is limited due to the limited availability of the elements incorporated in the precipitates, i.e., limited amounts of the precipitate forming elements. Thus, interparticle distances are much larger in case of the coarse precipitates eventually leading to lower flow stress.

Tensile samples being affected by all aforementioned features taken from the top side of the hat profiles were used for dynamic testing. Samples formed at tool temperatures up to $200 \text{ }^\circ\text{C}$ almost show the same mechanical behavior as the

AR T6 condition. In consequence, it can be deduced that all conditions up to that range are characterized by very similar initial microstructure, i.e., by the presence of well-distributed fine precipitates and only medium initial dislocation density. Thus, the T6 condition can be somehow preserved in these conditions. A higher forming tool temperature of $350 \text{ }^\circ\text{C}$ results in pronounced differences in microstructure evolution and, eventually, to a pronounced decrease in strength for both alloys studied. As detailed earlier, this can be rationalized based on low dislocation density and relatively large precipitates being further characterized by large interparticle distances.

At low strain rates, only the overall strength level is affected as can be deduced, e.g., from evaluation of the YS values. However, at high strain rates more significant differences are seen. Most importantly, SRS seems to be increased in case of the specimens processed in the cold tools. As data obtained in the course of the dynamic tensile tests, however, are characterized by machine-induced serrated flow and wavy propagation (due to oscillation of the test rig), evaluation of SRS is further accomplished based on analysis of data obtained by DIC. As is revealed by the analysis

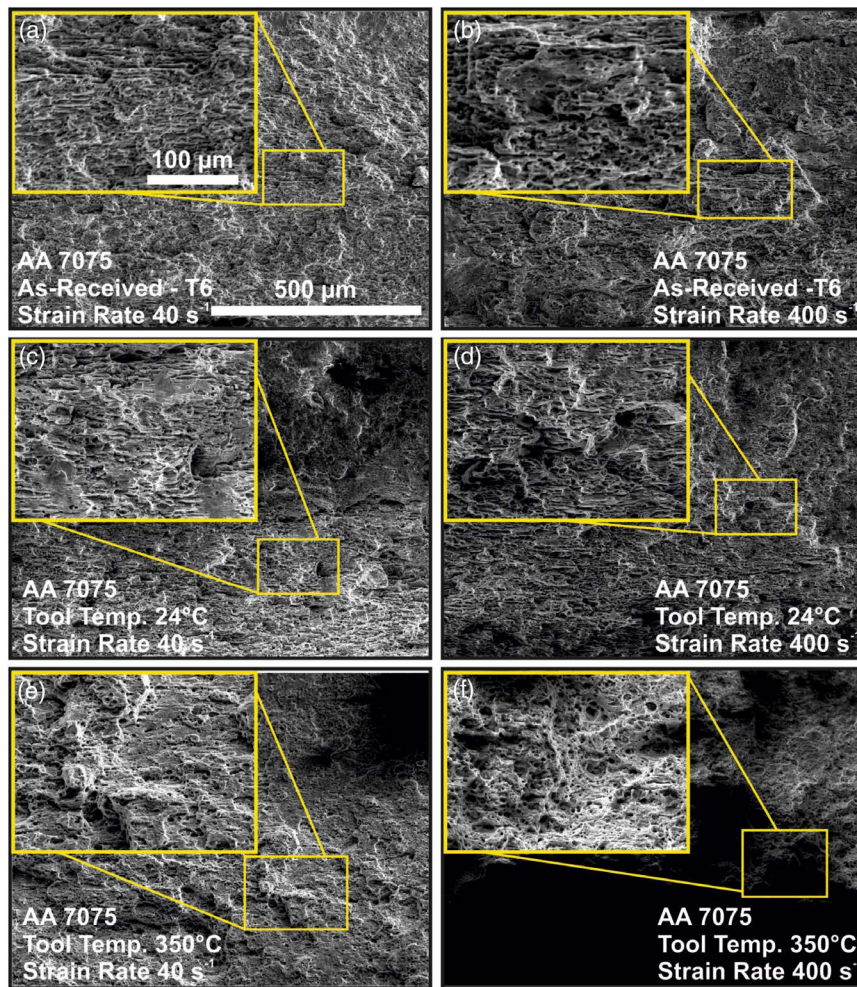


Figure 11. Fracture surfaces of AA7075 alloy in AR condition tested at a strain rate of a) 40 s^{-1} , b) 400 s^{-1} ; fracture surfaces of sample formed in the tempered tools at temperatures of c,d) 24°C and e,f) 350°C . Samples were tested at a strain rate of c,e) 40 s^{-1} , d,f) 400 s^{-1} (Pictures and insets show low and high magnifications, respectively.)

of strain field evolution, high strain rates lead to generally higher local strain values and a somehow more homogeneous strain pattern. In some cases, even the initiation of two necking regions is seen at the highest strain rate.

With increasing global plastic strain, i.e., shortly before failure, highest localized strain is observed in all specimens. In the range of strain rates considered, dynamic tensile deformation strongly promotes activity of dislocations and, thus, an increase in dislocation density. This intensifies dislocation–dislocation interaction as well as dislocation–precipitate interaction.^[89,92] It should be noted that the impact of dislocation–precipitate interaction on the overall mechanical response is different in parts formed with various tool temperatures as the precipitate sizes and morphologies can significantly affect the nature of interaction. In this regard, it is well-known that interaction between dislocations and fine and well-distributed precipitates causes a higher sensitivity to the rate of deformation.^[95] To experimentally substantiate the mechanisms and relationships introduced in this section, being assumed to be responsible for the differences seen in

the mechanical behavior under impact loading for the aluminum alloys in focus, in-depth microstructure analysis has to be conducted, e.g., by high-resolution transmission electron microscopy. Clearly, such analysis is beyond the scope of this work and, hence, will be subject of follow-up studies.

5. Conclusions

The dynamic tensile deformation behavior of two thermomechanically processed high-strength aluminum alloys, AA6082 and AA7075, at strain rates of 40, 200, and 400 s^{-1} was analyzed in this study. Forming of structures followed a novel processing route allowing for tailoring of microstructure using tempered tools. The following conclusion can be drawn based on the results shown: 1) Microstructural analysis revealed that grain sizes of both alloys remain relatively constant during thermomechanical processing. However, the formation of substructures takes place in case of the components formed and cooled in

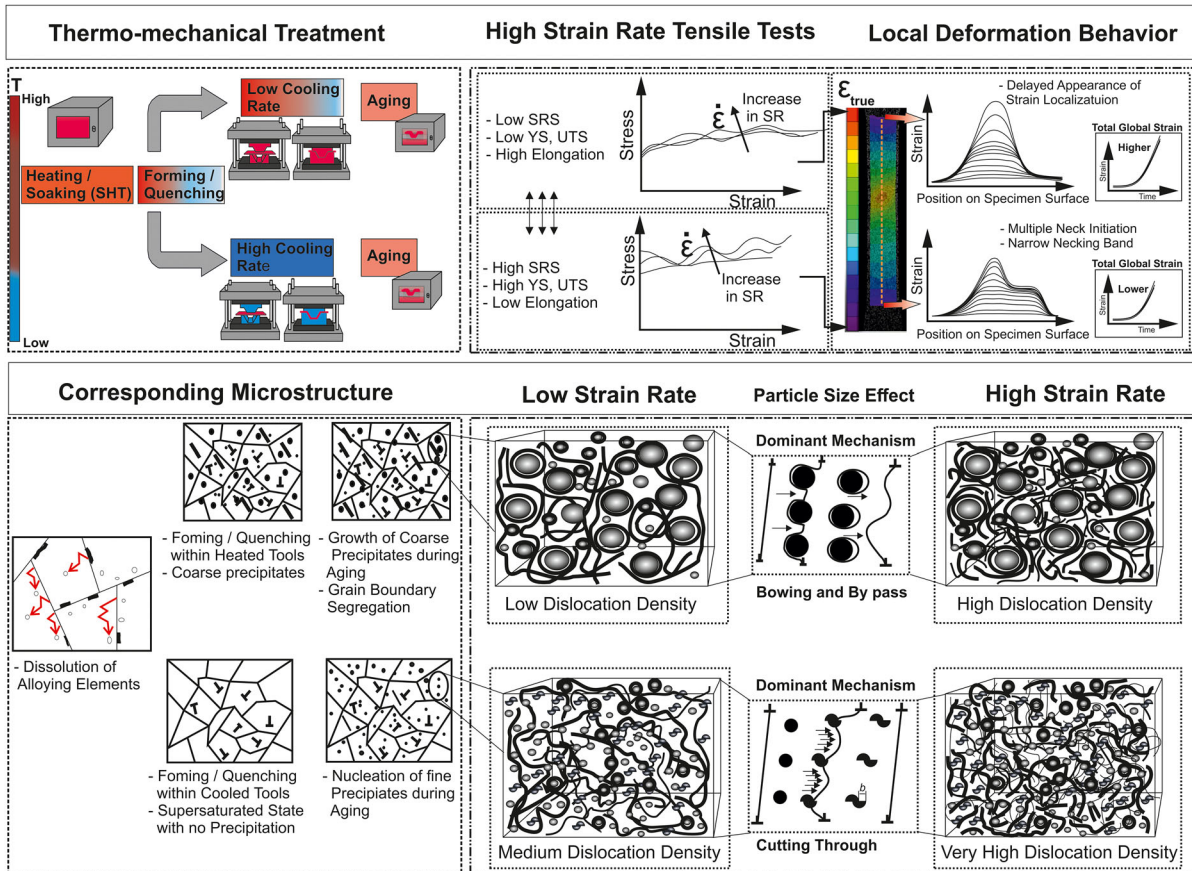


Figure 12. Schematic illustration detailing the microstructural evolution promoted by the thermomechanical process parameters as well as tensile deformation conditions.

the hot tool. Further SEM investigations via BSE contrast revealed that the differing tool temperatures considerably affect morphology and size of precipitates formed in the subsequent aging treatment. Segregation of large precipitates alongside the grain boundaries is found for the AA7075 alloy processed in the hot tool; 2) Dynamic tensile tests revealed an increase in yield strength, ultimate tensile strength, and plastic strain with increasing strain rates. In up to 200 °C tempered forming tools formed samples are characterized by almost the same mechanical properties as the AR T6 condition. A higher forming tool temperature of 350 °C leads to a significant decrease of strength of the material in the range of strain rates considered; 3) DIC analysis revealed a relatively homogenous local strain distribution along the gauge length up to necking for all thermomechanically treated conditions. Relatively high logarithmic strains are characteristic for the AR material. High deformation rates lead to a delay of appearance of strain localization and necking, respectively, eventually leading to higher global strain levels; 4) Fracture surfaces were characterized indicating the occurrence of ductile failure for both alloys within the examined range of strain rates. Fracture surfaces of the samples formed and cooled in the tool with a temperature of 350 °C consist of larger and deeper dimples compared with those processed in the cold tools.

Acknowledgements

The authors gratefully acknowledge financial support from the Hessen State Ministry for Higher Education, Research and the Arts—Initiative for the Development of Scientific and Economic Excellence (LOEWE) for the Project ALLEGRO (Subprojects A2, A3 and B1). Moreover, the authors thank Mr. Stefan Seidel and Andreas Suckau for sample preparation.

Conflict of Interest

The authors declare no conflict of interest.

Keywords

dynamic tensile deformation, high-strength aluminum alloys, hot forming, microstructures, thermomechanical processing

Received: February 18, 2020
Revised: April 21, 2020
Published online: May 28, 2020

- [1] E. A. Starke, J. T. Staley, *Prog. Aerosp. Sci.* **1996**, *32*, 131.
[2] W. J. Joost, P. E. Krajewski, *Scr. Mater.* **2017**, *128*, 107.

- [3] A. Poznak, D. Freiberg, P. Sanders, in *Fundamentals of Aluminium Metallurgy*, Woodhead Publishing, Cambridge, UK **2018**, pp. 333–386.
- [4] J. Hirsch, *Trans. Nonferrous Met. Soc. China* **2014**, *24*, 1995.
- [5] S. Rana, R. Figueiro, *Adv. Composite Mater. Aerosp. Eng.* **2016**, *1*, 1.
- [6] L. Zhu, N. Li, P. R. N. Childs, *Propul. Power Res.* **2018**, *7*, 103.
- [7] M. Maikranz-Valentin, U. Weidig, U. Schoof, H. Becker, K. Steinhoff, *Steel Res. Int.* **2008**, *79*, 92.
- [8] Y. Liu, L. Wang, B. Zhu, Y. Wang, Y. Zhang, *Procedia Manuf.* **2018**, *15*, 701.
- [9] L. Deng, X. Wang, J. Jin, L. Xia, *Procedia Eng.* **2017**, *207*, 2388.
- [10] J. Lin, T. Dean, R. Garrett, A. Foster (World Intellectual Property Organization International Bureau), WO2008059242, PCT/GB2007/004347, **2008**.
- [11] R. P. Garrett, J. Lin, T. A. Dean, *Int. J. Plast.* **2005**, *21*, 1640.
- [12] J. Zhou, B. Wang, J. Lin, L. Fu, *Arch. Civil Mech. Eng.* **2013**, *13*, 401.
- [13] E. Scharifi, D. Kuhnhen, A. Ademaj, U. Weidig, M. Oldenburg, B. Prakash, *Proc. 6th Int. Conf. Hot Sheet Met. Form. High-Performance Steel*, Warrendale AIST, Atlanta, GA **2017**, p. 683.
- [14] N. Li, Z. T. Shao, J. G. Lin, T. A. Dean, *Key Eng. Mater.* **2016**, *716*, 337.
- [15] A. Wang, K. Zhong, O. El Fakir, J. Liu, C. Sun, L. L. Wang, J. Lin, T. A. Dean, *Int. J. Adv. Manuf. Technol.* **2016**, *89*, 1339.
- [16] N. Li, M. S. Mohamed, J. Cai, J. Lin, D. Balint, T. A. Dean, *AIP Conf. Proc.* **2011**, *1353*, 1555.
- [17] L. Wang, M. Strangwood, D. Balint, J. Lin, T. A. Dean, *Mater. Sci. Eng.: A* **2011**, *528*, 2648.
- [18] H. Gao, T. Weng, J. Liu, C. Li, Z. Li, L. Wang, *MATEC Web Conf.* **2015**, *21*, 05007.
- [19] D. C. Ko, D. H. Ko, J. H. Kim, J. H. Park, *Adv. Mech. Eng.* **2017**, *9*, 1.
- [20] J. Zhou, B. Y. Wang, J. G. Lin, L. Fu, W. Y. Ma, *Trans. Nonferrous Met. Soc. China* **2014**, *24*, 3611.
- [21] A. C. L. Lam, Z. Shi, J. Lin, X. Huang, *Int. J. Mech. Sci.* **2015**, *103*, 115.
- [22] O. El Fakir, S. Das, I. Stone, G. Scamans, Z. Fan, L. Wang, D. Balint, J. P. Dear, J. Lin, in *Key Engineering Materials*, Vol. 622, Trans Tech Publications Ltd, Switzerland **2014**, pp. 596–602.
- [23] P. F. Bariani, S. Bruschi, A. Ghiotti, F. Michieletto, *CIRP Ann. Manuf. Technol.* **2013**, *62*, 251.
- [24] E. Hornbogen, A. Mukhopadhyay, E. Starke, *Scr. Metall. Mater.* **1992**, *27*, 733.
- [25] A. Foster, T. A. Dean, J. Lin, WO 2010/032002, **2009**.
- [26] X. Fan, Z. He, S. Yuan, P. Lin, *Mater. Sci. Eng.: A* **2013**, *587*, 221.
- [27] X. Fan, Z. He, S. Yuan, K. Zheng, *Mater. Sci. Eng.: A* **2013**, *573*, 154.
- [28] X. Fan, Z. He, K. Zheng, S. Yuan, *Mater. Des.* **2015**, *83*, 557.
- [29] S. J. Yuan, X. B. Fan, Z. Bin He, *Procedia Eng.* **2014**, *81*, 1780.
- [30] E. Scharifi, R. Knoth, U. Weidig, *Procedia Manuf.* **2019**, *29*, 481.
- [31] K. Zheng, J. Lee, W. Xiao, B. Wang, J. Lin, *Metals* **2018**, *8*, 231.
- [32] S. V. Sajadifar, G. Moeini, E. Scharifi, C. Lauhoff, S. Böhm, T. Niendorf, *J. Mater. Eng. Perform.* **2019**, *28*, 5255.
- [33] N. Li, J. Zheng, C. Zhang, K. Zheng, J. Lin, T. A. Dean, *MATEC Web Conf.* **2015**, *21*, 05015.
- [34] N. R. Harrison, S. G. Luckey, *SAE Int. J. Mater. Manuf.* **2014**, *7*, 2014.
- [35] *Mechanical Testing and Evaluation* (Eds: H. Kuhn, D. Medlin), ASM International, Materials Park, OH **2000**, p. 427.
- [36] X. Nie, B. Song, Y. Ge, W. W. Chen, T. Weerasooriya, *Exp. Mech.* **2009**, *49*, 451.
- [37] P. Zhang, Y. Wang, Y. Xie, Y. Zhou, *Vacuum* **2018**, *157*, 306.
- [38] S. L. Yan, H. Yang, H. W. Li, X. Yao, *J. Alloys Compd.* **2016**, *688*, 776.
- [39] A. S. Khan, H. Liu, *Int. J. Plast.* **2012**, *36*, 1.
- [40] R. Smerd, S. Winkler, C. Salisbury, M. Worswick, D. Lloyd, M. Finn, *Int. J. Impact Eng.* **2005**, *32*, 541.
- [41] J. R. Pothnis, Y. Perla, H. Arya, N. K. Naik, *J. Eng. Mater. Technol., Trans. ASME* **2011**, *133*, 1.
- [42] Y. Chen, A. H. Clausen, O. S. Hopperstad, M. Langseth, *Int. J. Solids Struct.* **2009**, *46*, 3825.
- [43] R. Bobbili, V. Madhu, A. K. Gogia, *J. Mater. Res. Technol.* **2016**, *5*, 190.
- [44] E. Cadoni, M. Dotta, D. Forni, H. Kaufmann, *Procedia Struct. Integr.* **2016**, *2*, 986.
- [45] O. S. Lee, G. H. Kim, M. S. Kim, J. S. Hwang, *KSME Int. J.* **2003**, *17*, 787.
- [46] E. El-Magd, M. Abouridouane, *Int. J. Impact Eng.* **2006**, *32*, 741.
- [47] X. Chen, Y. Peng, S. Peng, S. Yao, C. Chen, P. Xu, *PLoS One* **2017**, *12*, 1.
- [48] J. H. Chen, W. F. Xu, R. Z. Xie, F. J. Zhang, W. J. Hu, X. C. Huang, G. Chen, *Theor. Appl. Mech. Lett.* **2017**, *7*, 317.
- [49] T. Rahmaan, J. Noder, A. Abedini, P. Zhou, C. Butcher, M. J. Worswick, *Int. J. Impact Eng.* **2020**, *135*, 103390.
- [50] R. C. Dorward, K. R. Hasse, *J. Mater. Eng. Perform.* **1995**, *4*, 216.
- [51] T. Ye, Y. Wu, A. Liu, C. Xu, L. Li, *Vacuum* **2019**, *159*, 37.
- [52] L. Djapic Oosterkamp, A. Ivankovic, G. Venizelos, *Mater. Sci. Eng.: A* **2000**, *278*, 225.
- [53] F. Kabirian, A. S. Khan, A. Pandey, *Int. J. Plast.* **2014**, *55*, 232.
- [54] S. Yan, H. Yang, H. Li, X. Yao, *Int. J. Plast.* **2016**, *85*, 203.
- [55] M. Sasso, A. Forcellese, M. Simoncini, D. Amodio, E. Mancini, *Key Eng. Mater.* **2015**, *651–653*, 114.
- [56] H. Yamada, T. Kami, R. Mori, T. Kudo, M. Okada, *Metals* **2018**, *8*, 576.
- [57] N. Tian, G. Wang, Y. Zhou, K. Liu, G. Zhao, L. Zuo, *Materials* **2018**, *11*, 1533.
- [58] K. Chihab, Y. Estrin, L. P. Kubin, J. Vergnol, *Scr. Metall.* **1987**, *21*, 203.
- [59] T. Cheng, X. Xu, Y. Cai, S. Fu, Y. Gao, Y. Su, Y. Zhang, Q. Zhang, *Opt. Lasers Eng.* **2015**, *65*, 89.
- [60] A. Yilmaz, *Sci. Technol. Adv. Mater.* **2011**, *12*, 063001.
- [61] Y. C. Lin, H. Yang, D. G. He, J. Chen, *Mater. Des.* **2019**, *183*, 108122.
- [62] M. Härtel, C. Illgen, P. Frint, M. Wagner, *Metals* **2018**, *8*, 88.
- [63] O. S. Hopperstad, T. Børvik, T. Berstad, O. G. Lademo, A. Benallal, *Modell. Simul. Mater. Sci. Eng.* **2007**, *15*, 747.
- [64] J. Coër, P. Y. Manach, H. Laurent, M. C. Oliveira, L. F. Menezes, *Mech. Res. Commun.* **2013**, *48*, 1.
- [65] P. Zhou, Y. Song, L. Hua, J. Lu, J. Zhang, F. Wang, *Mater. Sci. Eng.: A* **2019**, *759*, 498.
- [66] Y. Choi, J. Lee, S. S. Panicker, H. K. Jin, S. K. Panda, M. G. Lee, *Int. J. Mech. Sci.* **2020**, *170*, 105344.
- [67] M. S. Mohamed, A. D. Foster, J. Lin, D. S. Balint, T. A. Dean, *Int. J. Mach. Tools Manuf.* **2012**, *53*, 27.
- [68] P. Larour, *Strain Rate Sensitivity of Automotive Sheet Steels: Influence of Plastic Strain, Strain Rate, Temperature, Microstructure, Bake Hardening and Pre-Strain*, Shaker Verlag GmbH, Aachen, Germany **2010**.
- [69] Y. Guo, Q. Ruan, S. Zhu, Q. Wei, H. Chen, J. Lu, B. Hu, X. Wu, Y. Li, D. Fang, *Phys. Rev. Lett.* **2019**, *122*, 015503.
- [70] Y. Ashuach, C. Avinadav, Z. Rosenberg, *EPJ Web Conf.* **2012**, *26*, 01047.
- [71] A. Eisenlohr, I. Gutierrez-Urrutia, D. Raabe, *Acta Mater.* **2012**, *60*, 3994.
- [72] C. Sachs, H. Fabritius, D. Raabe, *J. Struct. Biol.* **2006**, *155*, 409.
- [73] Z. Shao, J. Jiang, J. Lin, *J. Manuf. Processes* **2018**, *36*, 398.
- [74] F. J. Humphreys, M. Hatherly, *Recrystallization and Related Annealing Phenomena*, Elsevier, Amsterdam/New York **2004**.
- [75] M. W. Mahoney, C. G. Rhodes, J. G. Flintoff, W. H. Bingel, R. A. Spurling, *Metall. Mater. Trans. A* **1998**, *29*, 1955.
- [76] M. Reimann, J. Goebel, J. F. dos Santos, *Mater. Des.* **2017**, *132*, 283.
- [77] M. J. Starink, *Mater. Sci. Eng.: A* **2005**, *390*, 260.
- [78] P. V. Kumar, G. M. Reddy, K. S. Rao, *Def. Technol.* **2015**, *11*, 362.
- [79] J. Bonneville, B. Escaig, *Acta Metall.* **1979**, *27*, 1477.
- [80] T. Rasmussen, K. W. Jacobsen, T. Leffers, O. B. Pedersen, S. G. Srinivasan, H. Jónsson, *Phys. Rev. Lett.* **1997**, *79*, 3676.
- [81] S. I. Rao, D. M. Dimiduk, J. A. El-Awady, T. A. Parthasarathy, M. D. Uchic, C. Woodward, *Acta Mater.* **2010**, *58*, 5547.

- [82] M. Yaghoobi, G. Z. Voyiadjis, *Comput. Mater. Sci.* **2017**, *138*, 10.
- [83] M. Yaghoobi, G. Z. Voyiadjis, *Acta Mater.* **2018**, *151*, 1.
- [84] N. R. Barton, J. V. Bernier, R. Becker, A. Arsenlis, R. Cavallo, J. Marian, M. Rhee, H. S. Park, B. A. Remington, R. T. Olson, *J. Appl. Phys.* **2011**, *109*, 073501.
- [85] N. R. Barton, M. Rhee, *J. Appl. Phys.* **2013**, *114*, 123507.
- [86] E. Hornbogen, H. Warlimont, in *Metallkunde*, Springer Berlin Heidelberg, Berlin, Heidelberg **2001**, p. 251.
- [87] A. Lehtinen, L. Laurson, F. Granberg, K. Nordlund, M. J. Alava, *Sci. Rep.* **2018**, *8*, 1.
- [88] Y. Xiang, D. J. Srolovitz, L.T. Cheng, E. Weinan, *Acta Mater.* **2004**, *52*, 1745.
- [89] W. M. Lee, M. A. Zikry, *Int. J. Solids Struct.* **2012**, *49*, 3291.
- [90] K. Qin, L. M. Yang, S. S. Hu, *Chin. Phys. Lett.* **2009**, *26*, 076201.
- [91] Z. Xu, R. C. Picu, *Phys. Rev. B* **2007**, *76*, 094112.
- [92] R. C. Picu, R. Li, Z. Xu, *Mater. Sci. Eng.: A* **2009**, *502*, 164.
- [93] M. Huang, L. Zhao, J. Tong, **2011**.
- [94] F. H. Olivares, J. Gil Sevillano, *Acta Metall.* **1987**, *35*, 631.
- [95] R. J. Arsenault, S. Li, *Metall. Trans. A* **1989**, *20*, 1429.
- [96] Y. Guo, Z. Zhuang, X. Y. Li, Z. Chen, *Int. J. Solids and Struct.* **2007**, *44*, 1180.
- [97] Y. Fan, Y. N. Osetskiy, S. Yip, B. Yildiz, *Proc. Natl. Acad. Sci.* **2013**, *110*, 17756.
- [98] S. Mercier, N. Granier, A. Molinari, F. Llorca, F. Buy, *J. Mech. Phys. Solids* **2010**, *58*, 955.
- [99] J. W. Hutchinson, K. W. Neale, A. Needleman, in *Mechanics of Sheet Metal Forming*, Springer, US **1978**, p. 111.
- [100] H. Zhang, K. Ravi-Chandar, *Int. J. Fract.* **2006**, *142*, 183.
- [101] D. E. Grady, D. A. Benson, *Exp. Mech.* **1983**, *23*, 393.
- [102] S. Mercier, A. Molinari, *Int. J. Impact Eng.* **2004**, *30*, 403.
- [103] G. Besnard, F. Hild, J. M. Lagrange, P. Martinuzzi, S. Roux, *Int. J. Impact Eng.* **2012**, *49*, 179.
- [104] N. F. Mott, *Proc. R. Soc. London, Ser. A* **1947**, *189*, 300.
- [105] R. Bobbili, A. Paman, V. Madhu, *Mater. Sci. Eng.: A* **2016**, *651*, 753.
- [106] T. Chiyatan, V. Uthaisangsuk, *Mater. Sci. Eng.: A* **2020**, *779*, 139125.